



The taxonomy of graphite nanoplatelets and the influence of nanocomposite processing

Zheling Li ^a, Thomas J.A. Slater ^{b,1}, Xinyu Ma ^b, Yingjie Yu ^a, Robert J. Young ^{a,*}, Timothy L. Burnett ^{b,**}

^a National Graphene Institute and School of Materials, UK

^b Henry Moseley X-ray Imaging Facility and School of Materials, University of Manchester, Manchester, M13 9PL, UK

ARTICLE INFO

Article history:

Received 15 August 2018

Received in revised form

7 October 2018

Accepted 12 October 2018

Available online 12 October 2018

ABSTRACT

The reinforcement efficiency of graphene in a nanocomposite relies on the size, morphology, defects and agglomeration of flakes. However, the characterisation is usually undertaken only for the raw materials and any changes that take place during processing are not taken into consideration. In this work, epoxy nanocomposites reinforced by graphite nanoplatelet (GNP) were prepared and nano-scale X-ray computed tomography was used to visualize the geometry, morphology and defects of the flakes, as well as the three dimensional agglomerates that are normally difficult to characterise by other techniques. In combination with micromechanical analysis, the taxonomy of the nanoplatelets is shown to be of great importance in controlling the mechanical properties of nanocomposites, and this has been shown to explain the deviations of the predictions of micromechanical models from the measured values. Particularly, it is shown that taking single average values of flake size may not be appropriate and the entire distribution of flake size need to be taken into consideration. Furthermore, it is shown that the Young's modulus of a nanocomposite is controlled principally by a small number of large flakes and that volume average distributions of flake size are more appropriate to use rather than number average ones.

© 2018 The Authors. Published by Elsevier Ltd. This is an open access article under the CC BY license (<http://creativecommons.org/licenses/by/4.0/>).

1. Introduction

Graphene in the form of both flakes and nanoplatelets has shown huge potential for application in composites [1]. Apart from providing mechanical reinforcement [2], its high electrical and thermal conductivity also endow multifunctionality [1,3]. Another advantage is that it enables the tailoring of the composite properties that conventional fibre composites cannot provide [4,5]. On the other hand, however, due to the existing defects, low bending stiffness and also the poor interlayer adhesion of the graphene flakes, their morphology can be easily affected or damaged during preparation and processing [6–8].

From our knowledge of conventional fibre composites, the fibre diameter [9], length [10] and orientation [11,12] all play significant

roles in determining the mechanical properties of the composites. It has been demonstrated that this also applies to nanocomposites in that 2D fillers with larger lateral dimensions [13,14] and smaller thicknesses [15] tend to give better reinforcement, consistent with the micromechanical models, e.g. the rule of mixtures [16,17] and Halpin-Tsai model [18,19], that have been used to predict the mechanical properties of the nanocomposites. However, unlike microscale fibres, the characterisation of the physical properties of graphene as a reinforcement is quite limited.

Routinely the geometry of graphene can be characterised by atomic force microscope (AFM) [18,20] and transmission electron microscope (TEM) [18,20], but the measurements can be either time-consuming or not adequately representative and ignore the inevitable distributions in particle size. Some attempts have been made to undertake statistical analyses [21–23], such as the reports from Hu et al. [24] and Paton et al. [21]. This is often undertaken upon exfoliated flakes on a flat substrate or TEM grid, and the flakes will inevitably change after composite processing. Additionally, other physical properties such as the wrinkling and fracture of the flakes and agglomeration of the graphene can be very difficult to visualize in nanocomposites [25–28] which makes the analysis

* Corresponding author.

** Corresponding author.

E-mail addresses: robert.young@manchester.ac.uk (R.J. Young), timothy.burnett@manchester.ac.uk (T.L. Burnett).

¹ Present Address: Electron Physical Science Imaging Center, Diamond Light Source Ltd, Didcot, Oxfordshire, OX11 0DE, UK.

even harder to carry out. Some of these issues have been summarized by Fornes and Paul [4] in their review on clay-based polymer nanocomposites, however, a reliable and clear way of visualizing the nanoscale flakes and determining related physical properties is still of vital importance to explain any deviation of the measured mechanical properties of nanocomposites from the predictions by micromechanical models [18,22]. Recent work has demonstrated the use of X-ray computed tomography (CT) to observe GNP inside a rubber compound, but a more careful examination of the structure and morphology of the individual GNP flakes is still needed along with a detailed understanding of the taxonomy of the nanoplatelets [29,30].

In this work, the nanocomposite samples were prepared by adding different loadings of GNPs into an epoxy resin. Nanoscale X-ray CT was used to visualize the 'real' structure of individual GNP flakes in the nanocomposites including geometry, morphology, orientation, defects as well as any agglomeration. The mechanical properties of the nanocomposites were measured and the influence of the 'real' GNP structure on determining the mechanical properties of the nanocomposites is discussed. This is then used to interpret the relationship between the micromechanical predictions and the measured Young's modulus of the nanocomposites. This work is able to shed light on the influence of these crucial issues on the mechanical properties of the nanocomposites that are difficult to investigate and quantify by other experimental techniques.

2. Experimental

2.1. Materials

The GNP powder [31] was Grade M-25 supplied by XG Science (Michigan, USA). According to the supplier, its surface area is about 120–150 m²/g with an average thickness of 6–8 nm and a nominal diameter of around 25 μm, with density about 2.2 g/cm³ [32]. The epoxy resin and hardener used were Araldite LY and Aradur 5052 (Huntsman).

2.2. Sample preparation

The neat epoxy and nanocomposites with different GNP loadings of 0.1 wt%, 0.5 wt%, 1.0 wt% and 1.5 wt% were prepared as described previously [33], corresponding to a volume fraction of 0.06 vol% (~0.1 wt%), 0.3 vol% (~0.5 wt%), 0.6 vol% (~1.0 wt%) and 0.9 vol% (~1.5 wt%), respectively. For the neat epoxy sample, the hardener was added into epoxy resin with a weight ratio of 38:100 in a beaker at room temperature followed by magnetic stirring for 3–5 min. The mixture then was degassed at 40 °C until the bubbles were completely removed. After this the mixture was poured into moulds and left at room temperature for 24 h followed by another 4 h post-curing at 100 °C. The nanocomposites were prepared in a similar way, but the GNP powder was mixed with acetone (0.5 mg/ml) before being sonicated for 2.5 h. The epoxy was then added into the suspension and sonicated for another 2.5 h, followed by stirring overnight (~10 h). The mixture was weighed before and after stirring to ensure complete evaporation of the acetone, followed by degassing until the bubbles were fully removed. The hardener with the same weight ratio to the epoxy was then added before final degassing at 40 °C for around 20 min.

2.3. Mechanical testing

The mechanical properties of the nanocomposites were evaluated using tensile tests upon dumbbell specimens following ASTM D638 Type IV undertaken using an Instron 4301 mechanical testing

machine. The temperature and relative humidity of the laboratory was conditioned at 23 °C and 50%, respectively. The specimen gauge length was 10 mm and an extensometer was used to measure the extension precisely. The tensile testing rate was 0.5 mm/min. Two specimens were tested for the neat epoxy and at least 5 specimens were used for the nanocomposites with different GNP loadings.

2.4. X-ray computed tomography

The samples for X-ray CT were prepared by using a microtome (Leica Ultracut UC6 Ultramicrotome) and cut into a pyramid shape with the cross-sectional area at the top less than 0.1 mm × 0.1 mm. The data were collected by the Zeiss Xradia Ultra 810 instrument with a source energy 5.5 keV. The projections were acquired in the phase contrast mode and 'large field of view' mode. For each scan, 1201 projections were acquired over 180°, with a step size of 0.15°, and an exposure time of 20 s for each projection. 1 × binning was used for each scan, giving a pixel size of 32 nm. After the projections, the data were reconstructed using a filtered back-projection reconstruction through the Zeiss XMReconstructor software. Data were then visualized and quantified using the Avizo software package (version 9.2.0). A global threshold (different for all the four datasets due to the different intensity) was applied first to segment out the majority of the GNP flakes then the segmentation was adjusted manually to be more specific.

After the threshold procedure, the following step is needed to remove 'islands'. All the isolated 'islands' with sizes less than 150 pixels in 3D volume were removed as they were delaminated from large flakes. The 3D surface area and orientation of each flake in every sample was calculated. The 'Label Measures' function in Avizo was used to do the calculation for every flake. The 3D surface area measurement is a basic function of 'Label Measures' but determining flake orientation is more complicated and needs to be debugged manually. The orientation of each flake refers to the normal to the flake surface, the plane of which is defined by two orthogonal lines with one along the longest flake dimension.

2.5. Raman spectroscopy

Raman mapping was undertaken using a Renishaw InVia Raman system equipped with 488 nm laser. The laser spot size was about 2 μm and the step size for the mapping was 1.5 μm. Raman band shifts from the GNPs in the nanocomposites under strain were determined as described elsewhere using 633 nm laser excitation [29].

3. Results

3.1. X-ray computed tomography

An X-ray CT image showing an overview of the composite microstructure with a massive number of GNPs in the nanocomposites is shown in Fig. 1(a). X-ray CT offers a distinct advantage over other techniques, such as AFM and TEM where the GNPs are either on a substrate or confined in a very thin section of sample. X-ray CT enables the visualization of the 'real' morphology of GNPs in nanocomposite three-dimensionally. This allows us to understand how the morphology of GNP changes following the nanocomposites processing. Based on the measured surface area, an average length (diameter) of 2.2 ± 0.4 μm is calculated for the GNP flakes for both the 0.6 vol% and 0.9 vol% graphene loadings. The nominal size [32] and the size measured before nanocomposite processing [25] are also indicated in Fig. 1(b). Their lateral dimension enables the GNP flakes to be resolved even though their

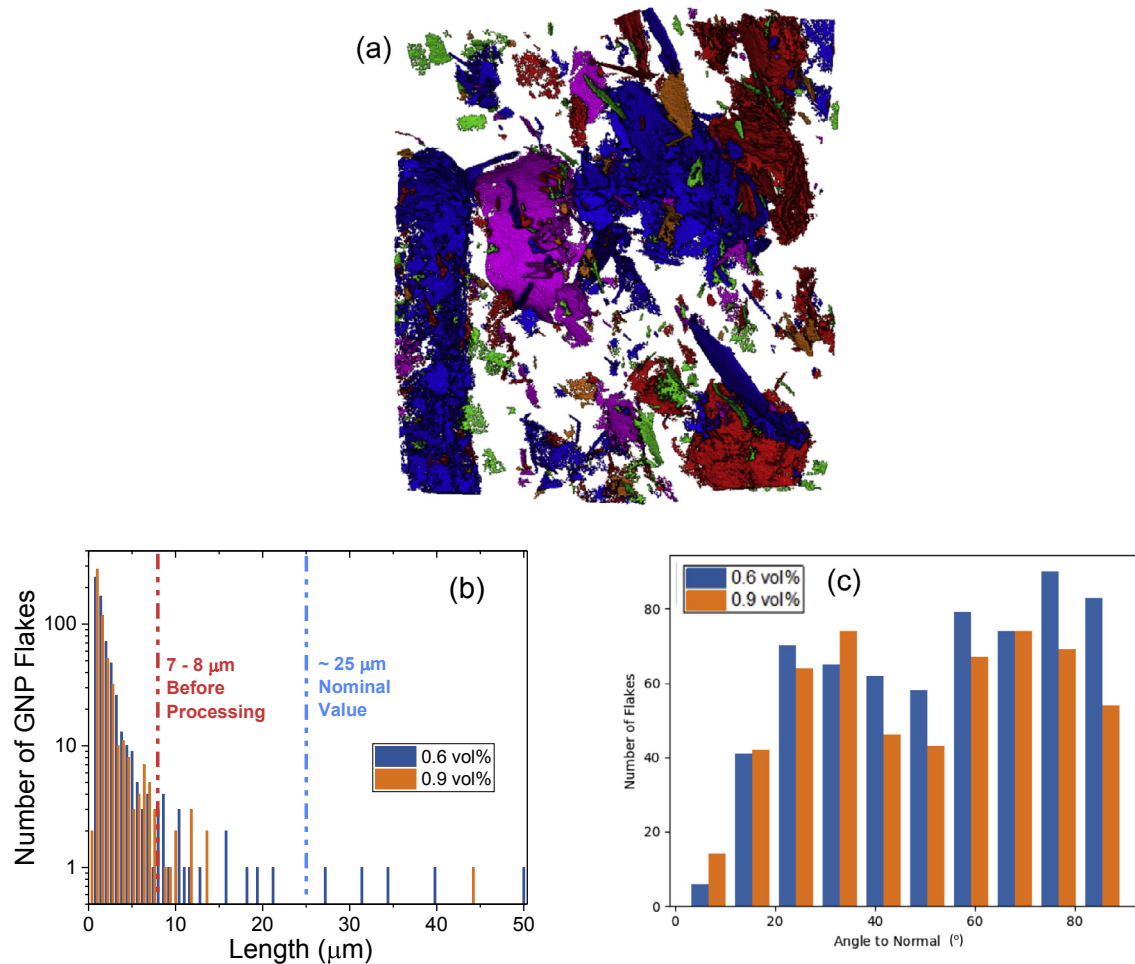


Fig. 1. (a) An X-ray CT image of a global view of the GNP flakes in the 0.6 vol% nanocomposite. (b) Number average distribution of the particles lengths (diameters) of more than 1000 particles in the 0.6 vol% and 0.9 vol% nanocomposites. The dashed blue and red lines indicate the lateral dimension at different stages of the nanocomposites processing. (c) The angles of the surface normal of the GNP flakes relative to the sample in the nanocomposites for 0.6 vol% and 0.9 vol% loading. (A colour version of this figure can be viewed online.)

thickness 6–8 nm is actually below the pixel size of the X-ray CT. However, these flake diameters are only $\sim 1/3$ of the original size as measured from the raw GNP powder ($\sim 7.7 \mu\text{m}$ [25]), showing a clear reduction in lateral size during the nanocomposite processing which involves both stirring and sonication of the GNP flakes in the resin. The measurements on the raw powder undertaken using SEM, however, may not be able to resolve the smallest flakes. Moreover the majority of the diameters determined from both the CT scans on the nanocomposites and SEM upon the raw powder are well below the nominal diameter of $25 \mu\text{m}$ quoted by the manufacturer for M25 GNPs [32]. The orientation of the flakes can also be measured using X-ray CT based on the direction of the normal of the GNP flakes. It can be seen in Fig. 1(c) that the GNP flakes are oriented randomly over the entire angle range in both the 0.6 vol% and 0.9 vol% nanocomposites.

In addition to being able to determine the size and orientation of the GNPs as they exist in the nanocomposites, it is possible to also resolve the individual GNPs and determine their basic characteristics. Based upon this approach it has been possible to undertake the analysis of the taxonomy of individual GNPs and classify them into different groups with similar characteristics.

The taxonomy is shown in Fig. 2 where the GNPs are classified into five broad groups. Fig. 2(a) shows an individual GNP around $20 \mu\text{m}$ in diameter with some damage around one edge but with a large uniform flat region over most of the flake. Fig. 2(b) shows two

curved flakes viewed edge on. Fig. 2(c) shows a flake that is so highly curved that it has fractured partially. A multi-layer flake is shown in Fig. 2(d) that consists of a stack of a number of individual layers. Finally, a large agglomerate of flakes is shown in Fig. 2(e). It will be demonstrated how the taxonomy of these GNPs can have a major effect upon their ability to reinforce nanocomposites.

3.2. Raman spectroscopy

Raman spectroscopy is another powerful technique for the characterisation of GNP nanocomposites. Fig. 3(a) shows the Raman spectra for the pure epoxy resin, the neat GNPs and the GNP/epoxy nanocomposite. The Raman bands for the GNPs can be clearly seen in the nanocomposite even though the loading is only 0.9 vol%. This is because of the strong resonance of the graphite forms of carbon [34].

The distribution of flakes in nanocomposites is often non-ideal as shown in Fig. 3 which can be confirmed quantitatively by mapping the surface of nanocomposites using Raman spectroscopy [35]. This can be undertaken by mapping the intensity ratio of the graphene Raman 2D band relative to that of an epoxy band (2925 cm^{-1}) as depicted in Fig. 3(a) [36] for the 0.06 vol%, 0.1 vol%, 0.3 vol%, 0.6 vol% and 0.9 vol%, GNP nanocomposites respectively (Fig. 3(b)–(f)). The red colour corresponds to the GNP-rich area and its proportion increases with the GNP loading, so that for the 0.9 vol

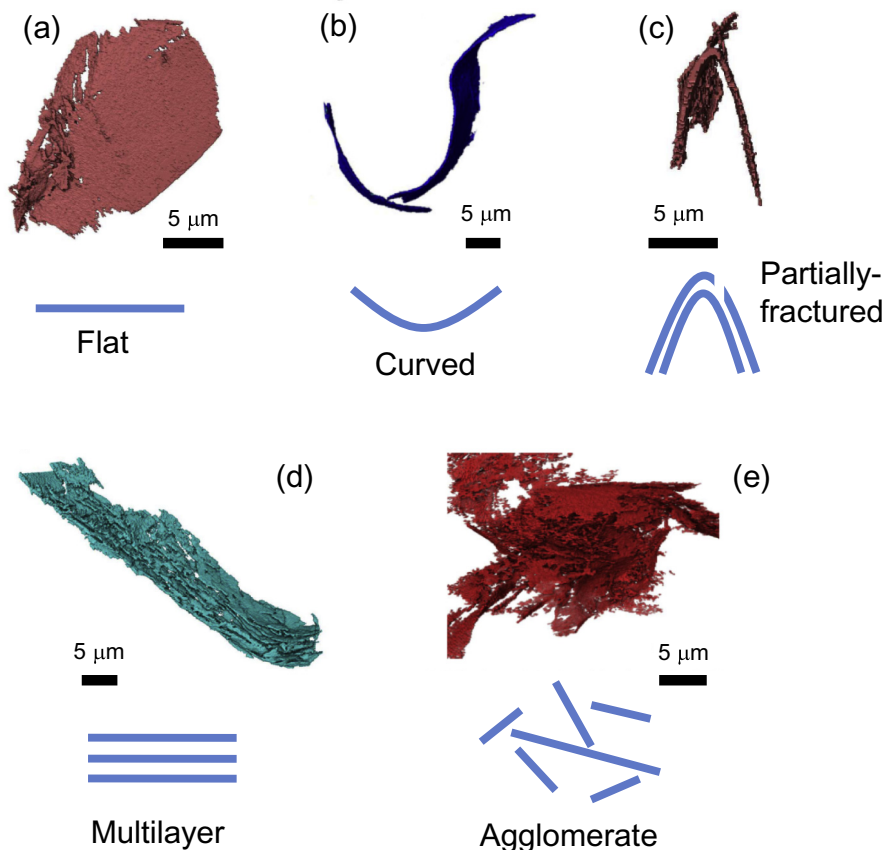


Fig. 2. X-ray CT images showing the taxonomy of individual GNP flakes in the 0.6 vol% ((a),(b) and (d)) and 0.9 vol% ((c) and (e)) nanocomposite along with schematic illustrations. (a) A flat flake. (b) Two curved GNP flakes. (c) A curved GNP flake that fractured partially in the middle. (d) A multi-layer flake with a large number of layers. (e) An agglomerate of flakes. (A colour version of this figure can be viewed online.)

% sample a high degree of agglomeration can be clearly seen. This suggests there is a good dispersion of GNP in the epoxy matrix at low GNP loading, but at higher loading, the GNPs tends to agglomerate [26,37]. The agglomeration is likely to occur between 0.6 and 0.9 vol% as can be found in Fig. 3, where in the 0.6 vol% sample GNPs were distributed quite uniformly but agglomerated at 0.9 vol%. However, it needs to be noted that agglomeration could still occur even at low loading but with a lower chance. The possible effects that the agglomeration has on the mechanical properties of the nanocomposites are: (1) the reduction of the area of surface that can interact with the matrix to provide stress transfer; (2) the cavities among the agglomerated structure can be too small for the resin to penetrate, especially one with high viscosity, and voids form accordingly [25].

3.3. Mechanical properties

The mechanical properties of the nanocomposites were determined for the different loading of GNPs in the nanocomposites. Fig. 4(a) shows the representative stress-strain curves for the neat resin and the four different loadings of GNPs. The Young's modulus of the nanocomposite E_c determined from the initial slope of the stress-strain curves is shown in Fig. 4(b) and it can be seen that it increases with the GNP loading from ~2.1 GPa of the neat epoxy to ~2.5 GPa of 0.3 vol% GNPs and then drops for higher loadings. In contrast, the ultimate tensile strength (UTS) and strain to failure decrease with the GNP loading, with the UTS decreasing from 70 MPa for the neat epoxy to 37 MPa for the sample with 0.9 vol% graphene loading, suggesting that the incorporation of GNP

agglomerates embrittles the nanocomposite.

It is possible to follow stress transfer from the epoxy resin matrix to the GNPs in nanocomposites from stress-induced Raman band shifts [29]. The 2D Raman band for GNPs is found to shift to a lower wavenumber under tensile deformation and the rate of shift (per unit strain) scales with the effective Young's modulus of the GNPs in the nanocomposite [29]. Fig. 4(c) shows the shift of the 2D band with strain for the 0.3 vol% nanocomposite giving a line with a slope of $-4.5 \text{ cm}^{-1}/\%$ strain. In contrast Fig. 4(d) shows that the band position for the nanocomposite with 0.9 vol% of GNPs does not appear to undergo any systematic change with strain and is scattered randomly.

4. Discussion

One of the simplest relationships that has been developed to describe the reinforcement achieved from a high-modulus particulate filler in a low-modulus matrix, under uniform strain, is the so-called "rule of mixtures" (RoM), in which the Young's modulus of a composite E_c is given by Refs. [16,17]:

$$E_c = E_f V_f + E_m (1 - V_f) \quad (1)$$

where E_f is the Young's modulus of the particulate filler, V_f is its volume fraction and E_m is the Young's modulus of the matrix. Fig. 4(b) shows the dependence of the Young's modulus of the nanocomposites as a function of the volume fraction of the GNPs. The filler modulus, E_f can be determined from the initial slope of the

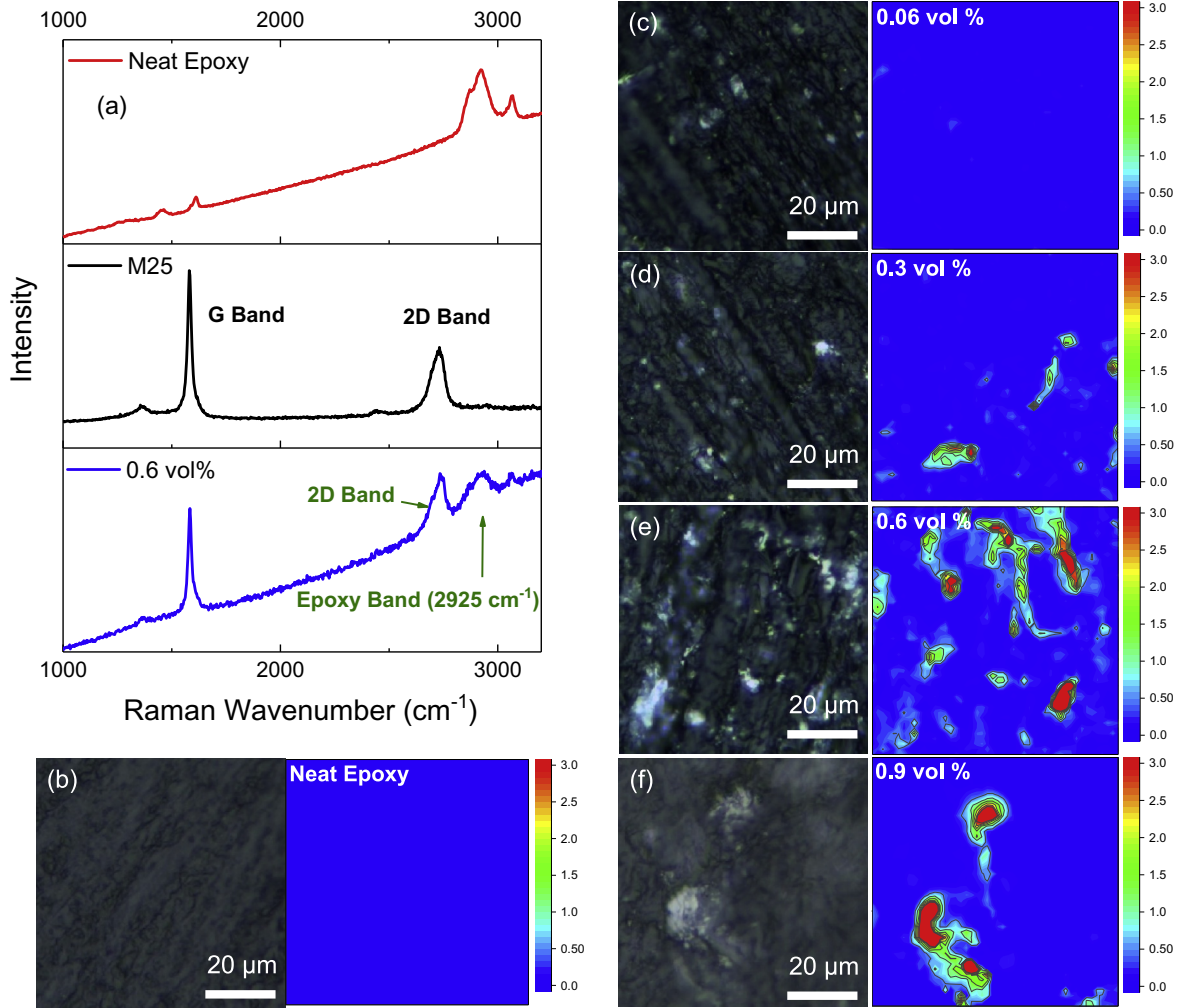


Fig. 3. (a) Raman spectra of GNPs, epoxy resin and the 0.6 vol% GNP nanocomposites. Optical image (left) and the Raman map of the same area (right) in (b) 0 vol % (neat epoxy resin), (c) 0.06 vol%, (d) 0.3 vol%, (e) 0.6 vol% and (f) 0.9 vol% GNP nanocomposites. (A colour version of this figure can be viewed online.)

line on a plot of E_c versus V_f and a value of 65 GPa is obtained for the GNPs up to 0.3 vol% loading.

It is also possible to determine the Young's modulus of the GNPs from the slope of the shift of the 2D Raman band with strain [29]. It is known that a pristine graphene monolayer with a Young's modulus of 1050 GPa undergoes a shift of $-60 \text{ cm}^{-1}/\%$ strain in tension [13]. Hence the shift rate of $-4.5 \text{ cm}^{-1}/\%$ strain measured in Fig. 4(c) for a GNP loading of 0.3 vol% corresponds to a GNP Young's modulus of $4.5 \times 1050/60 = 79 \text{ GPa}$ [38]. This is the same order as the value determined from the tensile testing and rule of mixtures. In general it is found that the Raman-derived values of E_f are usually slightly higher than those obtained from stress-strain data since the Raman spectra are often obtained from large aligned flakes [25].

It can be seen from Fig. 4(b) that above 0.3 vol% of GNPs the Young's modulus decreases with the further addition of GNPs. This is the result of agglomeration of the GNPs (Fig. 3) since the agglomerates no longer give effective reinforcement due to (1) the reduction of number of flakes that can reinforce and (2) voids and defects resulting from the agglomerates [25]. The consequences of this can also be seen in Fig. 4(d) where there is no well-defined Raman band shift upon deformation of the nanocomposite with a loading of 0.9 vol% GNPs.

In the case of nanocomposites containing particles such as GNP, Equation (1) can be modified by replacing E_f with $E_{\text{eff}}\eta_o\eta_l$ to take

into account the orientation of the reinforcing particles and their finite length to give:

$$E_c = E_{\text{eff}}\eta_o\eta_l V_f + E_m(1 - V_f) \quad (2)$$

where η_o is the Krenchel orientation factor [12,39] and η_l is the length factor [29]. The parameter E_{eff} is the effective Young's modulus of the filler that depends only upon its structure. The orientation factor η_o is 1 for aligned nanoplatelets and it was shown recently [12] that for randomly-oriented nanoplatelets, $\eta_o = 8/15$. It can, therefore, be taken as $\sim 8/15$ for the randomly-oriented GNPs in this present study. The length factor η_l ($0 \leq \eta_l \leq 1$) reflects the efficiency of stress transfer from the matrix to the filler that is controlled by both the shape of the filler and the strength of the filler-matrix interface. A recent study has shown that the length factor for GNPs is given by

$$\eta_l = \left[1 - \frac{\tanh(ns/2)}{ns/2} \right] \quad (3)$$

where $n = \sqrt{\frac{2G_m}{E_{\text{eff}}}} \left(\frac{t}{T} \right)$
 G_m is the shear modulus of the matrix, t is the nanoplatelet thickness and t/T is a geometric factor related to the volume

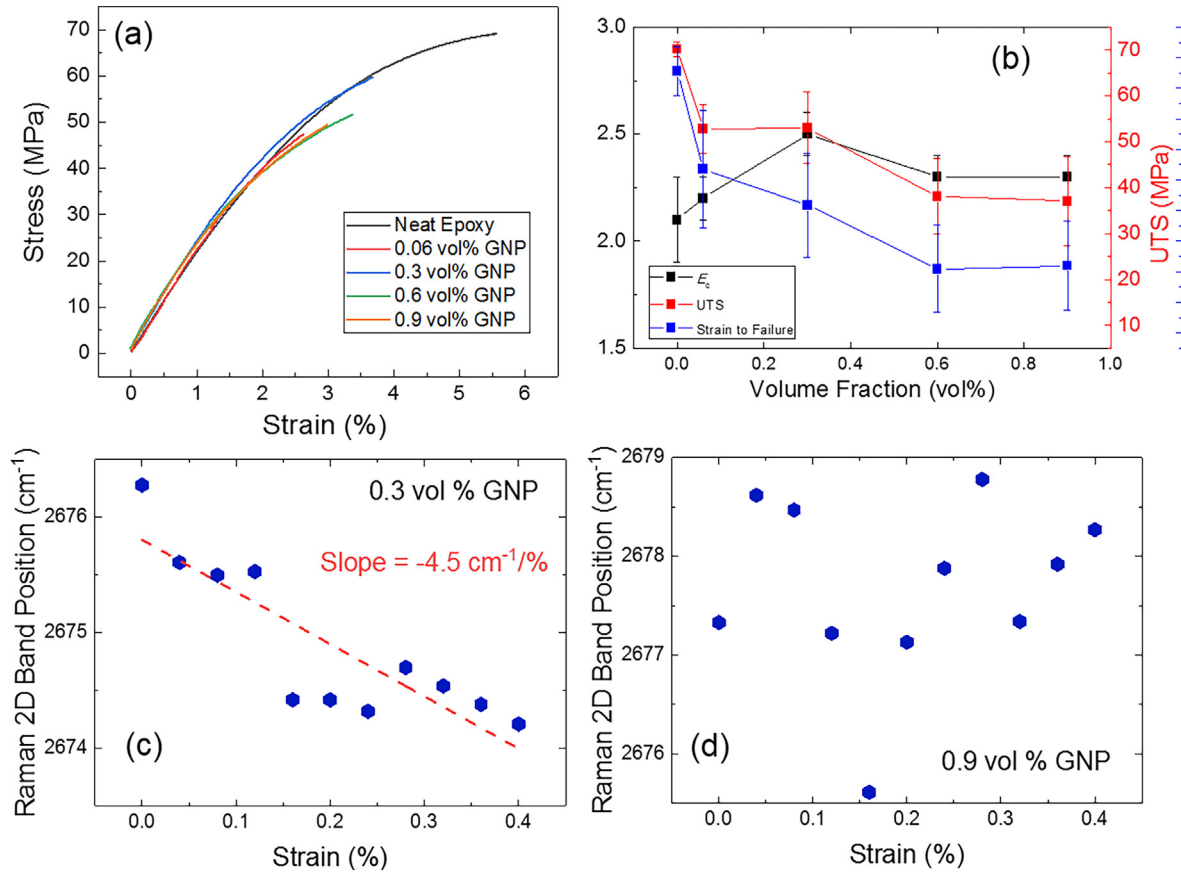


Fig. 4. (a) Representative stress-strain curves and (b) Young's modulus (black), UTS (red) and strain to failure (blue) of the nanocomposites with different GNP loadings. (c) The shift of the 2D Raman band of the GNPs as a function of strain for the 0.3 vol% nanocomposite. (d) The position of the 2D Raman band of the GNPs as a function of strain for the 0.9 vol% nanocomposite. (A colour version of this figure can be viewed online.)

fraction of the nanoplatelets and/or the strength of the nanoplatelets/matrix interface [25]. The parameter s is the nanoplatelet aspect ratio, its length (or diameter) divided by its thickness, l/t . If the microstructure of the nanocomposites is assumed to be nanoplatelets of thickness, t separated by matrix of thickness, T , then the volume fraction of graphene is given by $V_f = t/(t + T)$ and so $t/T = V_f/(1 - V_f) \sim V_f$ (for low loadings).

Most analyses of the mechanisms of reinforcement in composites assume that the reinforcing particles are all of the same size. It is clear, however, from Fig. 1 that there is a wide distribution of particle size and hence aspect ratio, s , in which case, therefore, average values have to be used. The determination of the average particle size, however, is not a trivial matter. It has similarities with considerations of the sizes of polydisperse polymer molecules where different average sizes are obtained depending upon whether they are averaged in terms of number or weight [16].

The distributions of particle size have been analysed for more than 600 GNP particles imaged in the CT scans in the epoxy composites. The distribution of the number of flakes in Fig. 1(b) shows that there is a large number of small flakes and that as the length increases the number of flakes decreases. The number average particle size is calculated to be about 2.2 μm . A very different picture is obtained when the volume distribution of the flakes is determined as shown in Fig. 5(a). Since the volume of the flakes increases as l^2 (assuming they are of uniform thickness) then this distribution is dominated by a small number of large flakes, the largest of which is 50 μm in length (diameter) as calculated from its surface area. In this case, the volume average particle size is an

order of magnitude higher than the number average at around 23 μm .

The length factor η_l defined in Equation (3) is strongly dependent upon the length of the flakes through the aspect ratio, s . The variation of η_l with l is also plotted in Fig. 5(a) and it can be seen that it falls from around unity for the large flakes to almost zero for the very small ones. Hence it means that in terms of reinforcement, the larger flakes have a much greater contribution to the Young's modulus of the nanocomposite through Equation (2). Moreover, since the larger flakes also occupy a higher proportion of the volume, these larger flakes will dominate the process of reinforcement. The above discussion suggests that large GNP flakes contribute more significantly to the reinforcement of nanocomposites, and a size reduction of at least 50%, may be expected during the nanocomposites processing.

More specifically, X-ray CT enables a detailed estimation of the Young's modulus by taking into account the contribution of each flake individually. Equation (2) can be modified to take into account the size of each GNP flake and the volume it occupies in the nanocomposites. For N particles it becomes:

$$E_c = E_{\text{eff}} \sum_{i=1}^N \eta_o^i \eta_l^i V_f^i + E_m (1 - V_f) \quad (4)$$

where i represents the parameter for the i th flake, $\eta_l^i = \left(1 - \frac{\tanh(ns_i/2)}{ns_i/2}\right)$, $n = \sqrt{\frac{2G_m}{E_{\text{eff}}}} \frac{V_f}{1 - V_f}$, $s_i = \frac{l_i}{t}$ and η_o^i , η_l^i and V_f^i are the

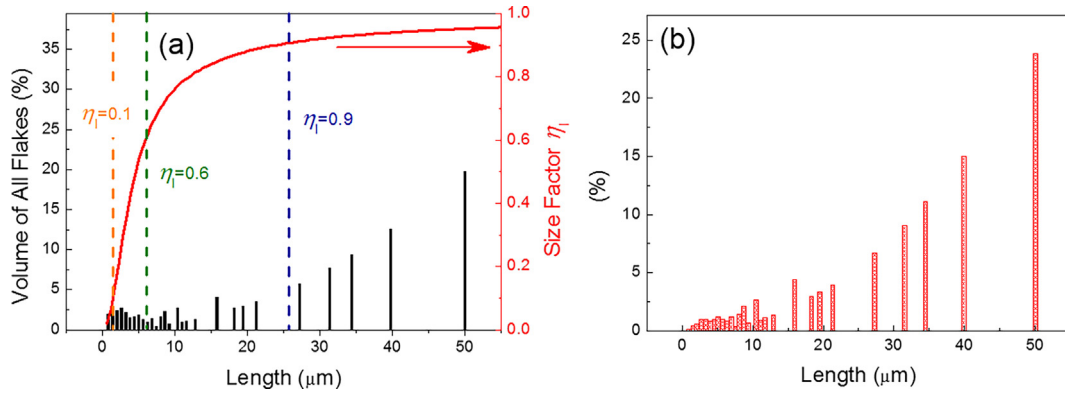


Fig. 5. Analysis from the CT scans of more than 600 different GNPs in the 0.6 vol% epoxy nanocomposites. (a) Distribution of the volume of flakes of different length (assuming they all square shaped with a thickness of 7 nm). (b) Proportion of the parameter A_i in ΣA_i for flakes of different length. (A colour version of this figure can be viewed online.)

Krenchel orientation factor, length factor and volume fraction for the i th flake. This equation shows the vital importance of the value of $\sum_{i=1}^N \eta_0^i \eta_l^i V_f^i$ in determining the reinforcement that fillers provide in a nanocomposite. In fact the parameter $A_i = \eta_0^i \eta_l^i V_f^i$ represents the reinforcing efficiency of each individual GNP and its proportion in ΣA_i is plotted in Fig. 5(b). It can be seen that the 3 largest flakes account for over 50% of ΣA_i . As it considers cumulatively all of GNP flakes in the matrix being studied, it overcomes the error that can be induced by using different ways of calculating the average values.

Finally, it is possible to model the effect of the volume fraction of GNPs upon the Young's modulus of the nanocomposites using the above equations as shown in Fig. 6. The two curves are for the values of Young's modulus determined from Equation (2) using either the number average or volume average values of flake lengths of 2.2 μm and 23 μm respectively to calculate η_l . The two red points are values of E_c calculated using Equation (4) using all the individual values of flake length. The flakes have been assumed to be oriented randomly ($\eta_0 = 8/15$) and the value of E_{eff} has been taken as 350 GPa for multilayer graphene [8,15]. Overall it can be seen that the volume average curve gives good agreement with the experimental values up to around 0.3 vol%, as opposed to the number average prediction. This is because the reinforcement (e.g.

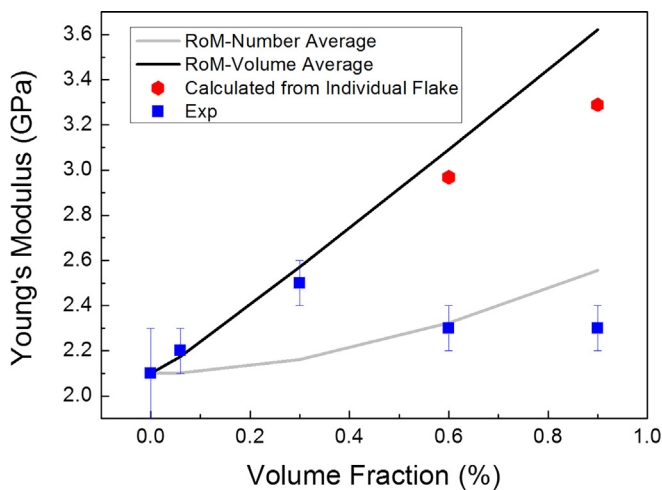


Fig. 6. The Young's modulus calculated by different methods and from experimental tensile testing. The blue squares are the experimental data and the error bars are the standard error of the mean. The number (grey) and volume (black) average values were determined using Equation (2) and Equation (4) was used to calculate the values for the individual flakes (parameters used were $E_{eff} = 350$ GPa, $\eta_0 = 8/15$ and $t = 7$ nm).

increase in Young's modulus) that GNP flakes can provide is characterised by A_i , the parameter reflecting their individual orientation, length factor and volume fraction as shown in Equation (4). Hence a large flake reinforces significantly better than a smaller one because it has both greater length factor as well as contributing a larger volume. This leads to another interesting prediction that, for a group of GNPs with given total volume and average lateral size (calculated using the commonly-used number average prediction), the wider their lateral size distribution, the better they should reinforce the composite, as a result of the greater contribution from the higher proportion of larger flakes. In Fig. 6, above the volume fraction of 0.3 vol% it appears that the agglomeration seen in Fig. 3 leads to a drop in Young's modulus. The apparent agreement with the theoretical curve for the number average at higher volume fractions is probably fortuitous. It is speculated that this may indicate the effect of agglomeration in reducing the effective size of GNP flakes [26].

5. Conclusions

Nanocomposites have been prepared by mixing GNPs with epoxy resin using different GNP loadings. It has been demonstrated that the use of nanoscale X-ray CT enables the visualization of the 'real' structure, such as morphology, defects and agglomeration of the GNP in nanocomposites. Combined with micromechanical analysis, these particular issues have been demonstrated to play significant roles on determining the mechanical properties of the nanocomposites. It has been found that the flake size of the GNPs is reduced after nanocomposite preparation, and that the reinforcement is dominated by a few large flakes. The wrinkling of GNP flakes has been visualized three-dimensionally in the CT scans which is otherwise very difficult to identify. The agglomeration of GNP flakes has also been visualized and its occurrence increases with GNP loading. All of these issues can explain the deviation between the measured mechanical properties and the micro-mechanical predictions. This work has shed light on the impact of some crucial issues on the mechanical properties of the nanocomposites that are normally difficult to observe and characterise and have not been investigated previously. Hence, it is suggested that a size reduction of at least a factor of two should be expected during the nanocomposites processing involving both stirring and sonication of the GNP flakes in the epoxy resin matrix.

Acknowledgements

The authors would like to acknowledge EPSRC funding for the

Henry Moseley X-ray Imaging Facility under grants EP/M010619, EP/K004530, EP/F007906, EP/F028431.7. HEFCE funding established the Multidisciplinary Characterization Facility and we are grateful for funding from UK Research Partnership Investment Funding (UKRPIF) Manchester RPIF Round 2. All the data used in this publication are available on request from the corresponding authors.

References

- [1] K. Hu, D.D. Kulkarni, I. Choi, V.V. Tsukruk, Graphene-polymer nanocomposites for structural and functional applications, *Prog. Polym. Sci.* 39 (11) (2014) 1934–1972.
- [2] D.G. Papageorgiou, I.A. Kinloch, R.J. Young, Mechanical properties of graphene and graphene-based nanocomposites, *Prog. Mater. Sci.* 90 (2017) 75–127.
- [3] M. Saeidjivash, J. Garg, B. Grady, B. Smith, Z. Li, R.J. Young, et al., High thermal conductivity through simultaneously aligned polyethylene lamellae and graphene nanoplatelets, *Nanoscale* 9 (35) (2017) 12867–12873.
- [4] T.D. Fornes, D.R. Paul, Modeling properties of Nylon 6/clay nanocomposites using composite theories, *Polymer* 44 (17) (2003) 4993–5013.
- [5] Y. Xu, W. Hong, H. Bai, C. Li, G. Shi, Strong and ductile poly(vinyl alcohol)/graphene oxide composite films with a layered structure, *Carbon* 47 (15) (2009) 3538–3543.
- [6] A. Zandiatashbar, G.-H. Lee, S.J. An, S. Lee, N. Mathew, M. Terrones, et al., Effect of defects on the intrinsic strength and stiffness of graphene, *Nat. Commun.* 5 (2014) 3186.
- [7] A.P. Rooney, Z. Li, W. Zhao, A. Gholinia, A. Kozikov, G. Auton, et al., Anomalous twin boundaries in two dimensional materials, *Nat. Commun.* 9 (2018) 3597.
- [8] Z. Li, I.A. Kinloch, R.J. Young, The role of interlayer adhesion in graphene oxide upon its reinforcement of nanocomposites, *Philos Trans Royal Soc A* 374 (2016), 20150283.
- [9] K. Young, F.M. Blighe, J.J. Vilatela, A.H. Windle, I.A. Kinloch, L. Deng, et al., Strong dependence of mechanical properties on fiber diameter for polymer–nanotube composite fibers: differentiating defect from orientation effects, *ACS Nano* 4 (11) (2010) 6989–6997.
- [10] Y. Huang, R.J. Young, Interfacial micromechanics in thermoplastic and thermosetting matrix carbon fibre composites, *Compos Part A Appl Sci* 27 (10) (1996) 973–980.
- [11] M.C. Andrews, R.J. Day, X. Hu, R.J. Young, Dependence of fibre strain on orientation angle for off-axis fibres in composites, *J. Mater. Sci. Lett.* 11 (20) (1992) 1344–1346.
- [12] Z. Li, R.J. Young, N.R. Wilson, I.A. Kinloch, C. Vallés, Z. Li, Effect of the orientation of graphene-based nanoplatelets upon the Young's modulus of nanocomposites, *Compos. Sci. Technol.* 123 (2016) 125–133.
- [13] L. Gong, I.A. Kinloch, R.J. Young, I. Riaz, R. Jalil, K.S. Novoselov, Interfacial stress transfer in a graphene monolayer nanocomposite, *Adv. Mater.* 22 (24) (2010) 2694–2697.
- [14] Z. Li, I.A. Kinloch, R.J. Young, K.S. Novoselov, G. Anagnostopoulos, J. Parthenios, et al., Deformation of wrinkled graphene, *ACS Nano* 9 (4) (2015) 3917–3925.
- [15] L. Gong, R.J. Young, I.A. Kinloch, I. Riaz, R. Jalil, K.S. Novoselov, Optimizing the reinforcement of polymer-based nanocomposites by graphene, *ACS Nano* 6 (3) (2012) 2086–2095.
- [16] R.J. Young, P.A. Lovell, *Introduction to Polymers*, third ed., CRC Press, Boca Raton, 2011.
- [17] R.J. Young, I.A. Kinloch, L. Gong, K.S. Novoselov, The mechanics of graphene nanocomposites: a review, *Compos. Sci. Technol.* 72 (12) (2012) 1459–1476.
- [18] J. Liang, Y. Huang, L. Zhang, Y. Wang, Y. Ma, T. Guo, et al., Molecular-level dispersion of graphene into poly(vinyl alcohol) and effective reinforcement of their nanocomposites, *Adv. Funct. Mater.* 19 (14) (2009) 2297–2302.
- [19] M.A. Rafiee, W. Lu, A.V. Thomas, A. Zandiatashbar, J. Rafiee, J.M. Tour, et al., Graphene nanoribbon composites, *ACS Nano* 4 (12) (2010) 7415–7420.
- [20] P. Song, Z. Cao, Y. Cai, L. Zhao, Z. Fang, S. Fu, Fabrication of exfoliated graphene-based polypropylene nanocomposites with enhanced mechanical and thermal properties, *Polymer* 52 (18) (2011) 4001–4010.
- [21] K.R. Paton, E. Varria, C. Backes, R.J. Smith, U. Khan, A. O'Neill, et al., Scalable production of large quantities of defect-free few-layer graphene by shear exfoliation in liquids, *Nat. Mater.* 13 (6) (2014) 624–630.
- [22] J. Shang, Y. Chen, Y. Zhou, L. Liu, G. Wang, X. Li, et al., Effect of folded and crumpled morphologies of graphene oxide platelets on the mechanical performances of polymer nanocomposites, *Polymer* 68 (2015) 131–139.
- [23] W. Gao, N. Zhao, W. Yao, Z. Xu, H. Bai, C. Gao, Effect of flake size on the mechanical properties of graphene aerogels prepared by freeze casting, *RSC Adv.* 7 (53) (2017) 33600–33605.
- [24] L.-H. Hu, F.-Y. Wu, C.-T. Lin, A.N. Khlobystov, L.-J. Li, Graphene-modified LiFePO₄ cathode for Lithium ion battery beyond theoretical capacity, *Nat. Commun.* 4 (2013) 1687.
- [25] R.J. Young, M. Liu, I.A. Kinloch, S. Li, X. Zhao, C. Vallés, et al., The mechanics of reinforcement of polymers by graphene nanoplatelets, *Compos. Sci. Technol.* 154 (2018) 110–116.
- [26] Z. Li, J. Chu, C. Yang, S. Hao, M.A. Bissett, I.A. Kinloch, et al., Effect of functional groups on the agglomeration of graphene in nanocomposites, *Compos. Sci. Technol.* 163 (2018) 116–122.
- [27] Y.T. Park, Y. Qian, C. Chan, T. Suh, M.G. Nejjad, C.W. Macosko, et al., Epoxy toughening with low graphene loading, *Adv. Funct. Mater.* 25 (4) (2015) 575–585.
- [28] S. Chandrasekaran, N. Sato, F. Tölle, R. Mülhaupt, B. Fiedler, K. Schulte, Fracture toughness and failure mechanism of graphene based epoxy composites, *Compos. Sci. Technol.* 97 (2014) 90–99.
- [29] J. Chu, R.J. Young, T.J.A. Slater, T.L. Burnett, B. Coburn, L. Chichignoud, et al., Realizing the theoretical stiffness of graphene in composites through confinement between carbon fibers, *Compos Part A Appl Sci* 113 (2018) 311–317.
- [30] S. Li, Z. Li, T.L. Burnett, T.J.A. Slater, T. Hashimoto, R.J. Young, Nanocomposites of graphene nanoplatelets in natural rubber: microstructure and mechanisms of reinforcement, *J. Mater. Sci.* 52 (16) (2017) 9558–9572.
- [31] A. Bianco, H.-M. Cheng, T. Enoki, Y. Gogotsi, R.H. Hurt, N. Koratkar, et al., All in the graphene family – a recommended nomenclature for two-dimensional carbon materials, *Carbon* 65 (2013) 1–6.
- [32] Technical Data Sheet XGnP Graphene Nanoplatelets - Grade M, XG Sciences, Ed, 2012.
- [33] C. Vallés, F. Beckert, L. Burk, R. Mülhaupt, R.J. Young, I.A. Kinloch, Effect of the C/O ratio in graphene oxide materials on the reinforcement of epoxy-based nanocomposites, *J. Polym. Sci., Part B: Polym. Phys.* 54 (2) (2016) 281–291.
- [34] A.C. Ferrari, D.M. Basko, Raman spectroscopy as a versatile tool for studying the properties of graphene, *Nat. Nanotechnol.* 8 (2013) 235–246.
- [35] S.A. Shojae, A. Zandiatashbar, N. Koratkar, D.A. Lucca, Raman spectroscopic imaging of graphene dispersion in polymer composites, *Carbon* 62 (2013) 510–513.
- [36] Z. Li, R.J. Young, R. Wang, F. Yang, L. Hao, W. Jiao, et al., The role of functional groups on graphene oxide in epoxy nanocomposites, *Polymer* 54 (21) (2013) 5821–5829.
- [37] F. Wang, L.T. Drzal, Y. Qin, Z. Huang, Mechanical properties and thermal conductivity of graphene nanoplatelet/epoxy composites, *J. Mater. Sci.* 50 (3) (2015) 1082–1093.
- [38] Z. Li, R.J. Young, I.A. Kinloch, Interfacial stress transfer in graphene oxide nanocomposites, *ACS Appl. Mater. Interfaces* 5 (2) (2013) 456–463.
- [39] Z. Li, R.J. Young, I.A. Kinloch, N.R. Wilson, A.J. Marsden, A.P.A. Raju, Quantitative determination of the spatial orientation of graphene by polarized Raman spectroscopy, *Carbon* 88 (2015) 215–224.